

Ocean Circulation on Enceladus With a High Versus Low Salinity Ocean

YAOXUAN ZENG ¹ AND MALTE F. JANSEN ²

¹*Department of Atmospheric and Oceanic Sciences, School of Physics, Peking University, Beijing 100871, China.*

²*Department of the Geophysical Sciences, University of Chicago, Chicago, IL 60637, USA.*

Submitted to PSJ

ABSTRACT

Previous studies that have considered the ocean circulation on Enceladus have generally assumed the salinity to be Earth-like. However, according to observations and geochemical constraints, the salinity of Enceladus' ocean is likely to be lower, and importantly, it is probably low enough to reverse the sign of thermal expansivity. We investigate the ocean circulation and stratification of Enceladus' ocean using a combination of theoretical arguments and simulations using the MITgcm. We find that, if the salinity is high, the whole ocean is unstratified, and convection dominates the entire ocean. However, if the salinity is low enough, there exists a stratified layer at the surface of the ocean. Such a layer can suppress the vertical flux of heat and tracers, thereby affecting the heat flux to the ice shell and leading to a vertical tracer mixing time scale in the stratified layer of at least hundreds of years. This time scale is inconsistent with a previous estimate of vertical ocean mixing of several years, based on the size of detected silica nanoparticles in the plumes, leading us to conclude that either the salinity of Enceladus' ocean is higher than previously suggested or the interpretation of silica nanoparticle observations has to be reconsidered.

Keywords: Enceladus — Ocean circulation — Stratified layer — Ocean heat transport — Tracer mixing time scale

1. INTRODUCTION

Strong evidence suggests that Enceladus maintains a global ocean (e.g., Patthoff & Kattenhorn (2011); Thomas et al. (2016)), and the possible existence of liquid water in contact with a rocky interior makes it a hot target in the search for life in the solar system. Understanding the ocean on Enceladus can also assist in understanding oceans on other icy moons in and outside the solar system, and help us better predict their habitability.

The ocean on Enceladus is estimated to be about 40 km in depth on average, and covered by a global ice shell (Thomas et al. (2016)). The ice shell is about 20 km deep on average, with the thickest part at the equator more than 30 km and the thinnest part at the south pole less than 10 km (Čadež

et al. (2019); Hemingway & Mittal (2019)). To maintain such a global ocean under the ice shell, as well as to explain the heat loss rate of around 10 GW in the south polar region (Spencer et al. (2006); Howett et al. (2011); Spencer et al. (2013)), there must be an energy source inside Enceladus.

The energy source is likely to be associated with tidal dissipation. In general, tidal dissipation is expected to occur in the ice shell, in the ocean, and in the solid core. However, tidal heating in the ocean is believed to be negligible compared to that in the ice shell and inner solid core (Chen & Nimmo (2011); Tyler (2011); Beuthe (2016); Hay & Matsuyama (2017)). The total tidal dissipation rate in the ice shell has recently been suggested to be on the order of 1 GW, with the maximum at the south pole where the ice shell is thinnest (Souček et al. (2019); Beuthe (2019)). Tidal dissipation in the ice shell has also been suggested as an explanation for the north-south asymmetry in the ice thickness (Kang & Flierl (2020)), as well as for the sustained plumes associated with the south-polar tiger stripes (Kite & Rubin (2016)). However, most of the tidal dissipation is likely to occur in the solid core, where it can reach $O(10 \text{ GW})$, and is believed to be strongest at the pole and weakest at the substellar and anti-substellar point at the equator (Choblet et al. (2017)). Tidal energy dissipation in the solid core will generate heat, which must be transported outwards to the ice shell by the ocean circulation.

Previous studies have looked into possible scenarios for the ocean circulation on Enceladus and other icy moons, with both ocean-only models and ice-ocean coupled models (e.g., Soderlund et al. (2014); Soderlund (2019); Amit et al. (2020); Ashkenazy & Tziperman (2020); Kang et al. (2020)). One characteristic feature of the ocean circulation on Enceladus may be hydrothermal convection columns which are expected to be aligned parallel to the rotation axis, and could extend from the sea floor to the ice-ocean interface (Goodman et al. (2004); Goodman & Lenferink (2012); Soderlund (2019); Ashkenazy & Tziperman (2020); Kang et al. (2020)). For another icy moon, Europa, hydrothermal convection plumes, quasi-3D turbulence, and baroclinic eddies have been suggested, based on different estimated parameter regimes, characterizing the strengths of the forcing that drives convection (Goodman et al. (2004); Goodman & Lenferink (2012); Soderlund et al. (2014)), as well as on whether salinity changes from freezing and melting are taken into consideration (Ashkenazy & Tziperman (2020)). Noting the substantial discrepancies among the simulations, the large uncertainty in external parameters, and the inherent computational challenges in modelling the global ocean in a realistic parameter regime, the ocean circulation regime on Enceladus remains uncertain.

All previous simulations of Enceladus' ocean assumed the salinity to be roughly similar to Earth's ocean and thus high enough that the thermal expansivity ($\alpha = -(1/\rho)(\partial\rho/\partial T)$) is always positive. However, the ocean on Enceladus is likely to be fresher than Earth's ocean. Although some studies have suggested the salinity to be higher than 20 g kg^{-1} based on dynamical considerations (e.g., Ingersoll & Nakajima (2016)), geochemical evidence and modelling suggest an upper limit for salinity of around 20 g kg^{-1} , dominated by NaCl, as in Earth's ocean (Glein et al. (2018)). If the salinity is less than 20 g kg^{-1} , the thermal expansivity of sea water is negative near the freezing point (Figure 1). In this case, a stably stratified layer may exist in the upper ocean on Enceladus, similar to a scenario that has been proposed for Europa by Melosh et al. (2004). To the best of our knowledge, no simulations have thus far been carried out to confirm the existence and effect of such a stably stratified layer.

Here we investigate the role of salinity on the dynamics of Enceladus' ocean, focusing in particular on the ocean's role in transporting heat and tracers from the sea floor to the ice shell. Ocean mixing can play a key role in transporting heat and constituents from the ocean-rock interface to the ice

shell, thus affecting ice melting as well as properties observable in plumes. According to the detected size of silica nanoparticles and the growth rate expected from Oswald ripening, the vertical mixing time scale has been estimated to be at most several years (Hsu et al. (2015)). One goal of this study is to analyze whether this vertical mixing time scale is consistent with the expected ocean circulation and transport on Enceladus. We carry out global ocean simulations using the 3D general circulation model MITgcm. Section 2 describes theoretical predictions for the ocean circulation on Enceladus. Section 3 shows results from numerical simulations. Section 4 provides concluding remarks.

2. THEORETICAL ANALYSIS

2.1. The Thermal Expansion Coefficient and Implications for Ocean Stratification

The equation of state for saltwater describes the density as a non-linear function of temperature (T), salinity (S), and pressure (P) (Jackett & McDougall (1995)). For salinities and pressures found in Earth's ocean, the density increases with salinity and decreases with temperature. Assuming a heat flux from the bottom due to tidal energy dissipation in the rocky interior, convection may then be expected in the whole ocean. As a result, the ocean would likely be well-mixed with very small temperature gradients (Figure 2(a)), consistent with the simulation results of Soderlund (2019), Ashkenazy & Tziperman (2020), and Kang et al. (2020).

However, for low enough temperature and salinity (and at the modest pressures expected on Enceladus), the thermal expansion coefficient, α , is negative, such that density increases with temperature. Under such circumstance, a critical temperature, T_c , exists at which the density of water reaches a maximum at a given salinity and pressure (Figure 1). In this regime, heating from below will not trigger convection until the temperature is heated above T_c . However, the temperature at the upper boundary will be kept at the freezing point, T_f , due to the surface ice shell. A stably stratified layer is thus expected to form in the upper ocean, where the thermal expansion coefficient is negative and

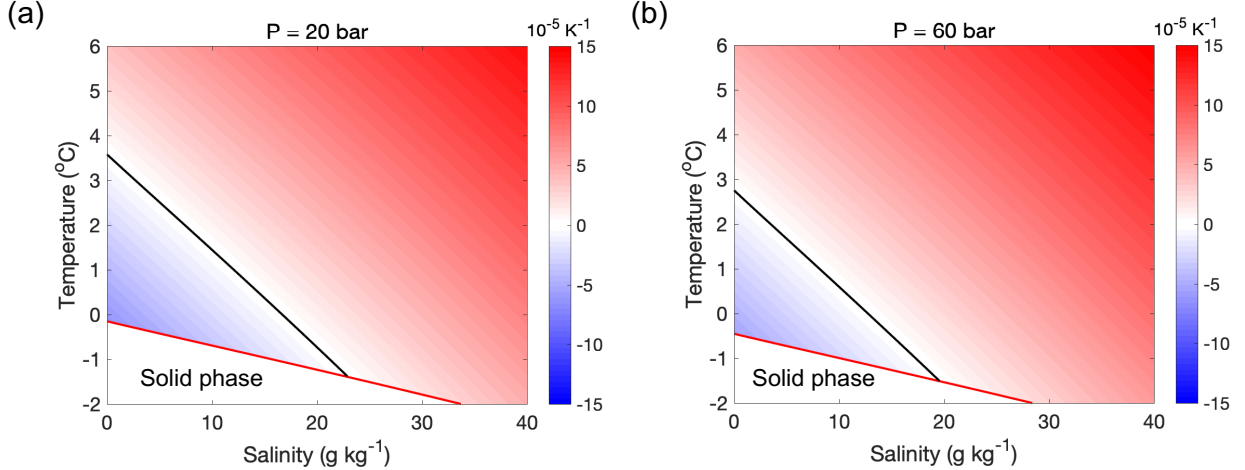


Figure 1. Thermal expansivity $\alpha = -(1/\rho)(\partial\rho/\partial T)$ of sea water as a function of salinity and temperature at (a) 20 bar and (b) 60 bar pressure, representative of the top and bottom of Enceladus' ocean. The black line indicates the zero contour. The red line indicates the freezing point T_f of sea water as a function of salinity. The area below the black line is where thermal expansivity of sea water is negative. The salinity at the intersection of the black and red lines is the maximum salinity for which negative α can exist under the given pressure. The calculation of the density is based on Jackett & McDougall (1995), and the calculation of the freezing point is based on Fofonoff & Millard Jr (1983).

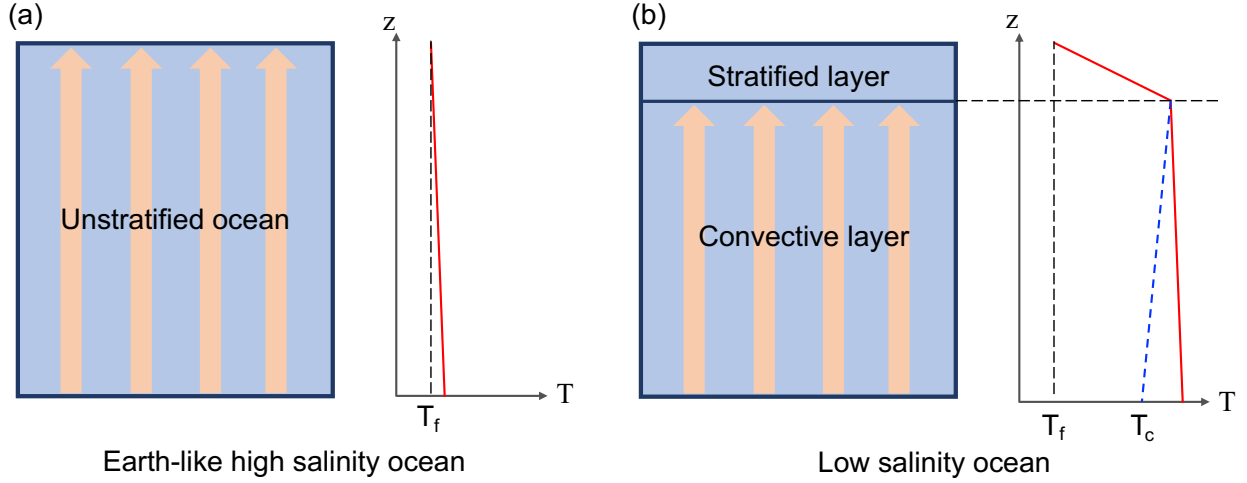


Figure 2. Schematic for the expected vertical structure of the ocean on Enceladus with different salinities. (a) and (b) show the vertical structure and temperature profile of high and low salinity oceans, respectively. Red lines indicate the temperature profile, and the blue dashed line in (b) indicates the critical temperature T_c , which decreases as pressure increases. The high salinity ocean is expected to be virtually unstratified, with convection throughout the ocean and a small negative vertical temperature gradient around the freezing point. In the low salinity ocean, we expect two layers: the upper stratified layer with linear vertical temperature profile, and the lower convective layer that has a weak vertical temperature gradient. The temperature at the interface between these two layers is at the critical temperature T_c , where the thermal expansion coefficient changes sign.

the temperature decreases upwards from T_c to T_f . This is similar to the stratified layer that has been hypothesized to exist in the ocean of Europa under the low salinity assumption by Melosh et al. (2004), although we note that the lower gravity and hence lower pressures on Enceladus make the conditions more favorable for the existence of a stably stratified layer. Below the stratified layer, the temperature is above T_c so that the thermal expansivity is positive. This layer is expected to be qualitatively similar to the high salinity scenario and we expect it to be characterized by convection. The temperature at the interface between these two layers should be near the critical temperature T_c . A schematic for the expected vertical stratification in a low salinity ocean is shown in Figure 2(b).

Since convection cannot occur in the stratified layer, the vertical heat flux is expected to be dominated by diffusion. We can then estimate the depth of the stratified layer using the equation of heat diffusion, $Q = c_p \rho \kappa_{z,heat} \partial T / \partial z$, where Q is the vertical heat flux, c_p is the heat capacity, ρ is the density of the water, and $\kappa_{z,heat}$ is the vertical thermal diffusion coefficient. Given the temperature contrast across the stratified layer, $\Delta T = T_f - T_c$, we can estimate the depth of the stratified layer H as

$$H = \frac{c_p \rho \kappa_{z,heat} |\Delta T|}{Q}. \quad (1)$$

If we assume the total bottom heating to be around 20 GW (Choblet et al. (2017)), the mean vertical heat flux is $Q \approx 0.03 \text{ W m}^{-2}$ at the top of the ocean. If we further assume the salinity to be 8.5 g kg^{-1} for Enceladus' ocean (Glein et al. (2018)), we find $T_f \approx -0.6^\circ\text{C}$, $T_c \approx 1.4^\circ\text{C}$, so that $|\Delta T| \approx 2.0 \text{ K}$. If we use the magnitude of the molecular thermal diffusivity, around $10^{-7} \text{ m}^2 \text{ s}^{-1}$, the depth of the stratified layer is $H \approx 30 \text{ m}$. In general, vertical mixing in the ocean can

be intensified through turbulence, in which case the molecular diffusivity should be replaced by the turbulent diffusivity. If we take the magnitude of the turbulent diffusivity in Earth's ocean, around $10^{-5} \text{ m}^2 \text{ s}^{-1}$ (Munk & Wunsch (1998)), the depth of the stratified layer would be $H \approx 3 \text{ km}$. The question of whether and by how much vertical mixing in the ocean of Enceladus is enhanced by turbulence is hence important and is discussed in the following section.

2.2. Tidal Dissipation and Turbulent Mixing in a Stratified Ocean

Vertical mixing in a stably stratified ocean increases the potential energy of the water column as buoyancy is fluxed downward, and hence requires a source of energy. In Earth's ocean, the turbulent kinetic energy that drives vertical mixing of the stratified water column is derived from wind stress and tidal dissipation (e.g. Wunsch & Ferrari (2004)). Wind stress cannot play a role on Enceladus due to the global ice shell and thin atmosphere, and tidal dissipation in the ocean is likely to be relatively weak on Enceladus. The tidal dissipation in the ocean on Enceladus is suggested to be 10^1 - 10^4 W , based on different models (Chen et al. (2014); Matsuyama et al. (2018); Hay & Matsuyama (2019)). This allows us to estimate the vertical turbulent diffusivity based on the energy required to mix a stably stratified ocean (e.g. Wunsch & Ferrari (2004); Yang et al. (2017)):

$$\kappa_z = \frac{\Gamma \varepsilon}{\rho N^2}. \quad (2)$$

Here κ_z is the vertical turbulent diffusivity, ε is the turbulent kinetic energy dissipation per unit volume, Γ is the “mixing efficiency”, i.e. the fraction of the kinetic energy dissipation that contributes to the generation of potential energy, and N is the Brunt-Väisälä frequency. Given that $N^2 = -(g/\rho_\theta)(\partial\rho_\theta/\partial z) \approx \alpha g \Delta T/H$ where ρ_θ is potential density and g is gravity, we have

$$\kappa_z = \frac{\Gamma \varepsilon H}{\rho g \alpha \Delta T} = \frac{\Gamma E}{\alpha \rho g \Delta T A}, \quad (3)$$

where E is the total energy input by tides and A is the horizontal area, and hence $\Gamma E/A$ is the energy used for vertical mixing per unit area, in units of W m^{-2} . If we assume Γ to be $\approx 20\%$ (Wunsch & Ferrari (2004)), then $\Gamma E/A$ is around 3×10^{-12} to $3 \times 10^{-9} \text{ W m}^{-2}$. Following the estimate in Section 2.1 for the conditions in the stratified layer of the low salinity ocean, we get $\alpha \approx -4 \times 10^{-5} \text{ K}^{-1}$, where we assumed a pressure of 20 bar and a temperature near the freezing point, and $\Delta T \approx -2.0 \text{ K}$. We can then estimate κ_z to be around 3×10^{-10} to $3 \times 10^{-7} \text{ m}^2 \text{ s}^{-1}$. By comparing these results with the vertical molecular diffusivity, which is around $10^{-7} \text{ m}^2 \text{ s}^{-1}$ for heat and $10^{-9} \text{ m}^2 \text{ s}^{-1}$ for tracers, we find that the vertical diffusion of temperature in the stratified layer of a low-salinity ocean is unlikely to be significantly enhanced by turbulence, while tracer mixing may be enhanced by up to two orders of magnitude, depending on the assumed value for tidal energy dissipation.

2.3. Conceptual Models of Ocean Heat Transport

To illustrate the role of ocean dynamics for the transport of heat from the rocky core to the ice shell, we here discuss three conceptual models of ocean heat transport that may be relevant in different parameter regimes. We consider three key transport processes: “slantwise convection” (convection along surfaces of constant angular momentum—here assumed to be parallel to the rotation axis), radial diffusion/mixing, and horizontal diffusion/mixing.

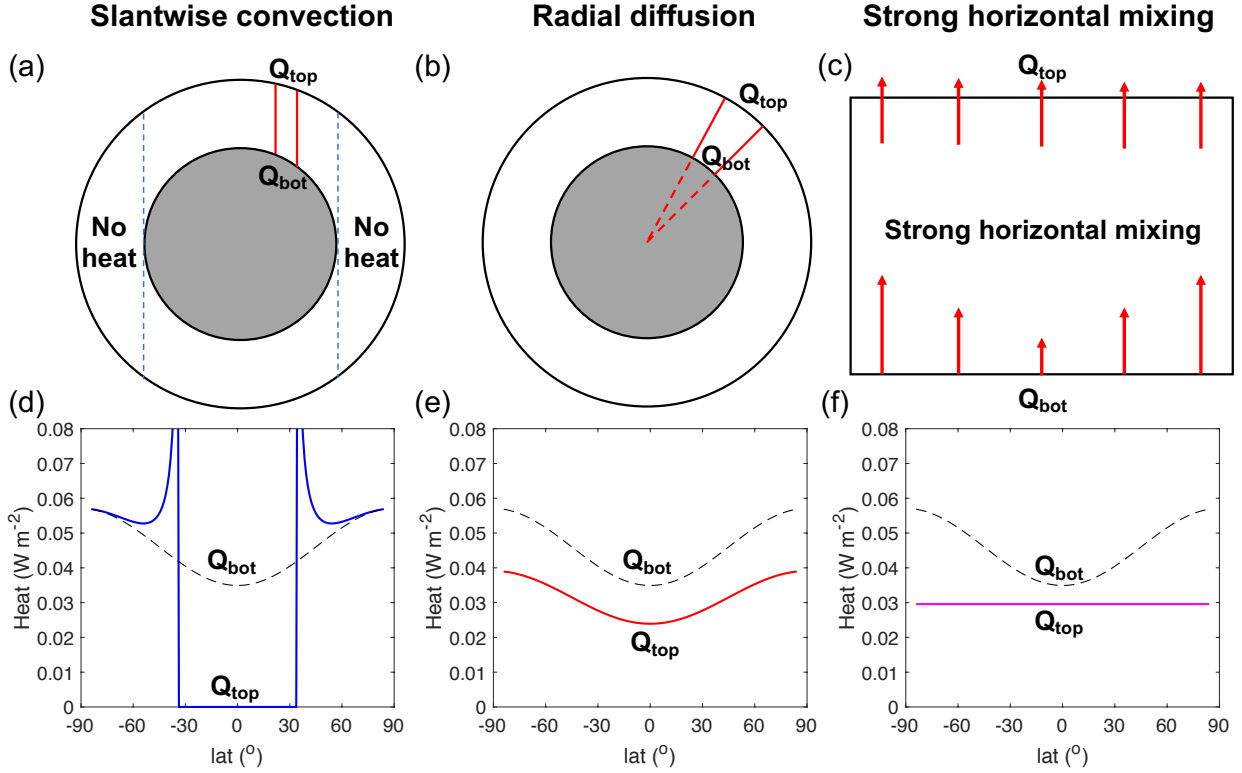


Figure 3. Three idealized models of ocean heat transport. (a)-(c) are schematics and (d)-(f) are the expected bottom and surface heat fluxes in the three models: “slantwise” convection, radial diffusion, and strong horizontal mixing, respectively. In (d)-(f), the dashed lines indicate the prescribed bottom heat fluxes and the solid lines indicate the surface heat fluxes. For more details on the calculation of the surface heat fluxes, see APPENDIX A.

The first model is the “slantwise convection” model. On Enceladus, convection is likely to be parallel to the rotation axis—or more generally along surfaces of constant total angular momentum (Goodman et al. (2004); Goodman & Lenferink (2012); Soderlund (2019); Kang et al. (2020)). For the “slantwise convection” model, we therefore assume that heat is transported vertically inside convective columns which are parallel to the rotation axis (Figure 3(a)). Inside the tangent cylinder that encircles the solid core (the blue dashed lines in Figure 3(a)), the heat flux is then calculated by matching the bottom heat flux to the corresponding area at the ice-ocean interface. At the intersection of the tangent cylinder and the ocean surface, the heat flux to the ice interface diverges in this model, because heat from a finite bottom area is transported to an infinitesimal surface area. Outside the tangent cylinder (at low-latitudes), there is no heat flux at the surface of the ocean since slantwise convective columns, following the axis of rotation, cannot reach the surface there (Figure 3(d)). To the best of our knowledge, a vanishingly small heat flux to the ice shell at the equator has not been observed in any existing simulations of icy moon oceans, as convective “rolls” are generally found to efficiently transport heat outwards near the equator (e.g., Cardin & Olson (1994); Christensen (2002); Kang et al. (2020)), although the lowest Ekman number simulation in Soderlund (2019) does show relatively weak radial heat transport at low latitudes. Whether the substantial low-latitude heat flux in existing simulations is robust, or related to limited resolution and unrealistic viscosities in the numerical models, remains an open question.

The second model is the “radial diffusion” model. This model is expected to be relevant if heat transport is dominated either by 3-dimensional turbulence or by molecular diffusion, i.e. any process that leads to an approximately isotropic diffusive transport. If the depth of the ocean is relatively small compared to the horizontal scale over which the heating at the bottom varies, the heat flux is then expected to be dominated by the radial diffusion component. In this limit, the pattern of the heat flux at the top of the ocean will match the bottom heat flux, reduced by a constant factor to account for the differences between the area at the bottom and the surface (Figure 3(b) & (e)).

The third model is the “strong horizontal mixing” model. If horizontal mixing is very efficient (e.g. due to the presence of geostrophic turbulence), any gradients in the deep ocean heating should be homogenized by ocean mixing and a relatively uniform surface heat flux is expected (Figure 3(c)). Under this circumstance, the surface heat flux should be equal to the average of the bottom heat flux everywhere (Figure 3(f)).

The heat flux to the surface ice shell is likely to play a role in determining the ice thickness distribution. With more heat transported to the surface at the pole than at the equator (the “slantwise convection” and “radial diffusion” models), ice is likely to be melting at the pole but forming at the equator. This heat flux pattern is therefore qualitatively consistent with the observed ice thickness distribution, and is also qualitatively similar to the heat flux in the low Ekman number simulation of Soderlund (2019), which is likely to be most representative of the regime expected to be found on Enceladus (c.f. Figure 3(e) in Soderlund (2019)). With strong horizontal ocean heat transport (the “strong horizontal mixing” model), the thickness of the ice shell may be expected to be uniform (Ashkenazy et al. (2018)). This heat flux pattern is qualitatively similar to that found in the simulations of Europa’s ocean in Ashkenazy & Tziperman (2020). The “strong horizontal mixing” model is arguably least consistent with the observation that the ice shell is thicker at the pole than the equator on Enceladus (Čadek et al. (2019); Hemingway & Mittal (2019)). However, the ice thickness variations can also be shaped by tidal dissipation in the ice shell itself (e.g. Kang & Flierl (2020)); the relative contribution of the two heat sources—tidal heating in the ice versus tidal heating from the core transported through the ocean—remains poorly constrained.

2.4. Vertical Tracer Mixing Time Scale

In the high salinity regime, geochemical tracers and small particles can be transported from the bottom to the surface of the ocean through convective processes relatively effectively. The vertical velocity in a rotating plume can be estimated as $w \sim \sqrt{B/f}$, where $B = g\alpha Q/\rho c_p$ is the buoyancy flux and $f \approx 1 \times 10^{-4} \text{ s}^{-1}$ is the Coriolis parameter (Jones & Marshall (1993)). The convective mixing time scale is then estimated to be

$$\tau_{conv} \sim \frac{D}{w} = \left(\frac{D^2 f}{B}\right)^{1/2}, \quad (4)$$

where $D \approx 40 \text{ km}$ is the depth of the ocean. If we assume the thermal expansivity α to be $4 \times 10^{-5} \text{ K}^{-1}$ and use $Q \approx 0.03 \text{ W m}^{-2}$, we find $\tau_{conv} \approx 70 \text{ years}$.

However, in the low salinity regime, there is no convection in the stratified layer, where vertical transport of tracers is achieved mainly by diffusion (either turbulent or molecular). As a result, the vertical mixing time for tracers from the bottom rocky core to the surface in the low salinity ocean is determined by the vertical diffusion time in the stratified layer.

The vertical diffusion equation is

$$\frac{\partial C}{\partial t} = \frac{\partial}{\partial z}(\kappa_{z,tracer} \frac{\partial C}{\partial z}), \quad (5)$$

where C is the tracer concentration and $\kappa_{z,tracer}$ is the vertical diffusivity of the tracer. Through scaling analysis of Equation (5), we find the diffusive mixing time scale

$$\tau_{diff} \sim \frac{H^2}{\kappa_{z,tracer}} = (\frac{c_p \rho |\Delta T|}{Q})^2 \frac{\kappa_{z,heat}^2}{\kappa_{z,tracer}}, \quad (6)$$

where we used Equation (1) to estimate the depth of the stratified layer H . We choose $Q \approx 0.03 \text{ W m}^{-2}$ and $|\Delta T| \approx 2.0 \text{ K}$ for a salinity of 8.5 g kg^{-1} , following Section 2.1. Using the range for thermal and tracer vertical diffusivity estimated in Section 2.2, we find the maximum mixing time scale to be $\tau_{diff}^{max} \approx 2 \times 10^4$ years when $\kappa_{z,heat} = 10^{-7} \text{ m}^2 \text{ s}^{-1}$ and $\kappa_{z,tracer} = 10^{-9} \text{ m}^2 \text{ s}^{-1}$ are both given by the molecular diffusivities, and the minimum time scale to be $\tau_{diff}^{min} \approx 200$ years when $\kappa_{z,heat} = \kappa_{z,tracer} = 10^{-7} \text{ m}^2 \text{ s}^{-1}$, i.e. the tracer diffusivity is enhanced by turbulent mixing to a similar value as the molecular thermal diffusivity. Vertical mixing through the stratified layer is therefore expected to take at least hundreds, and possibly up to tens of thousands of years.

3. NUMERICAL SIMULATIONS

3.1. Experimental Design

We perform numerical simulations using the Massachusetts Institute of Technology General Circulation Model (MITgcm) to solve the non-hydrostatic equations for a Boussinesq fluid in a rotating spherical shell, where all sphericity terms are preserved, including all components of the Coriolis force (see MITgcm Manual, Adcroft et al. (2018) and APPENDIX B). Radius, rotation rate and gravity are set to be the same as Enceladus (Table 1), and vertical variation of gravity is also taken into consideration (Figure 4(a), see APPENDIX B).

At the bottom of the ocean, we apply a fixed bottom heat flux pattern, following the zonal-mean tidal forcing pattern in Choblet et al. (2017) with a total flux of 20 GW (Figure 4(b), see APPENDIX B). The bottom heat flux boundary condition is qualitatively similar to that in Kang et al. (2020) and Ashkenazy & Tziperman (2020), but differs from Soderlund (2019) who applies fixed and uniform

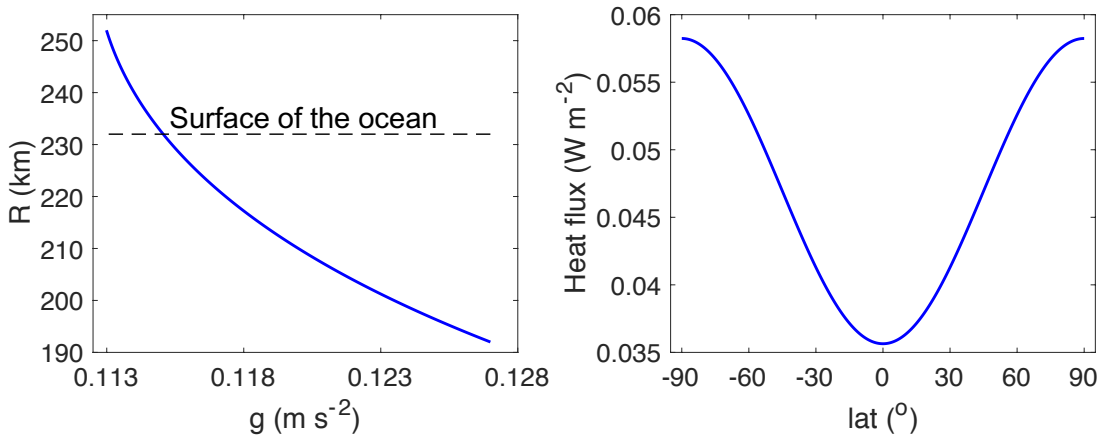


Figure 4. Gravity and bottom heating pattern of simulations. (a) Vertical gravity profile. The black dashed line indicates the radius at the surface of the ocean. (b) Bottom heat flux. Note that there is no zonal variation in the heat flux.

Table 1. Parameters of Enceladus

Parameters	Value
Surface gravity $g(r_s)$	0.113 m s^{-2}
Ice shell surface radius r_s	252 km
Ocean surface radius r_o	232 km
Ocean bottom radius r_c	192 km
Rotation rate Ω	$5.31 \times 10^{-5} \text{ s}^{-1}$
Prandtl number $Pr = \nu/\kappa$	10

NOTE—The values are taken from Čadež et al. (2019) with some simplifications.

bottom and surface temperatures. The prescribed bottom heat flux is better constrained from tidal models and observations than the bottom temperature distribution and provides a key constraint on the energetics of the circulation (Jansen (2016)). We apply a linear bottom drag such that the velocity at the bottom is relaxed to zero with a rate of 10^{-7} s^{-1} . The choice of a linear dissipation at the bottom is similar to Kang et al. (2020), and also practically similar to Ashkenazy & Tziperman (2020) who apply a no-slip bottom boundary condition together with vertical viscosity, but is different from Soderlund (2019) who applies stress-free boundary conditions. We believe that some bottom drag is preferable as it provides a physical constraint on the bottom zonal flows, which, in equilibrium, cannot impart any net angular momentum to the rocky core.

At the top model layer, we apply a linear restoring of temperature towards the freezing point T_f (-2°C for salinity of 35 g kg^{-1} and -0.6°C for salinity of 8.5 g kg^{-1}) with a restoring time of 1 month (30 Earth days). Our upper boundary condition can implicitly capture the heat exchange between the surface global ice shell and the ocean, but the fresh water flux and brine rejection associated with melting and freezing are not included in our simulations. Salinity changes associated with freezing and melting at the surface of the ocean can change the density of sea water, thus further affecting ocean circulation. A pole-to-equator overturning circulation driven by salinity gradients, which in turn are caused by ice formation at low-latitudes and melting at the pole, has been suggested in Lobo et al. (2020) and has also been found in coupled ice-ocean simulations using the MITgcm with a uniform ice thickness (Ashkenazy & Tziperman (2020); Kang et al. (2020)). Although freezing and melting at the bottom of the ice shell is likely to affect the ocean circulation, it is important to note that such forcing cannot energetically drive a circulation unless melting (which reduces the density) happens at a higher pressure (i.e. greater depth) than freezing (e.g. Wunsch & Ferrari (2004)). Instead, to counter the effect of the ice flow, melting needs to occur where the ice shell is thin (i.e. at small depth), while freezing would have to occur where the ice shell is thick. The salinity forcing then cannot drive a circulation but instead acts to stabilize the stratification in regions where the ice shell is relatively thin. The energy source for the global overturning circulation in Lobo et al. (2020), and the “salt-driven” circulation in the simulations of Ashkenazy & Tziperman (2020) and Kang et al. (2020), comes from parameterized turbulent vertical mixing where the ocean is stably stratified. As discussed in Section 2.2, mixing of a stratified ocean requires a supply of turbulent kinetic energy,

Table 2. Simulation Settings

Case	Salinity	$\kappa_{h,heat}$	$\kappa_{z,heat}$	Horizontal
Descriptions	(g kg ⁻¹)	(m ² s ⁻¹)	(m ² s ⁻¹)	Resolution
<i>HSaniso</i>	35	0.25	5×10^{-5}	$1^\circ \times 0.95^\circ$
<i>HSiso</i>	35	0.25	0.25	$1^\circ \times 0.95^\circ$
<i>HSiso05</i>	35	0.1	0.1	$0.5^\circ \times 0.475^\circ$
<i>LSaniso</i>	8.5	0.25	5×10^{-5}	$1^\circ \times 0.95^\circ$

which is likely to be very small on Enceladus. In how far a strong “salt-driven” circulation is possible on Enceladus thus remains an open question, which is here left for future work.

We simulate a 40 km deep ocean over a zonal range of 15° and meridional range from 85.5°S to 85.5°N . We are not simulating all longitudes to save computational resources and the poles are masked with land to ensure numerical stability. The vertical resolution is 1000 m. The horizontal resolution is 1° in the zonal and 0.95° in the meridional direction in most simulations, which is around $4 \text{ km} \times 4 \text{ km}$ near the equatorial surface. This horizontal resolution is not sufficient to resolve single convective columns. The expected minimum horizontal scale of the convective columns can be estimated using the length scale where rotation becomes important: $l_r \sim B^{1/2} f^{-3/2} \approx 0.2 \text{ m}$ (Jones & Marshall (1993)), which is many times smaller than the horizontal resolution. This indicates that in our simulations, convection is affected by the resolution and the parameterized turbulent diffusivities and viscosities, a situation that is unavoidable in global-scale simulations, where resolutions of $O(0.1 \text{ m})$ are computationally impossible to achieve. In order to provide at least some insight into how resolution can affect the simulation results, we perform one additional simulation with a finer horizontal resolution of 0.5° in the zonal and 0.475° in the meridional direction.

The horizontal turbulent diffusivity applied in our models is $0.25 \text{ m}^2 \text{ s}^{-1}$ in most simulations for numerical stability, and is decreased to $0.1 \text{ m}^2 \text{ s}^{-1}$ in the high horizontal resolution simulation following Kolmogorov scaling (see APPENDIX B). The turbulent vertical diffusivity is likely to be small in the stratified layer of the low salinity ocean, as discussed in Section 2.2. For the low salinity ocean we therefore use an anisotropic diffusion with a smaller vertical diffusivity set to $\kappa_z = 5 \times 10^{-5} \text{ m}^2 \text{ s}^{-1}$. This value is still larger than suggested by the estimate in Section 2.2, but was chosen here to ensure numerical stability and to be able to explicitly resolve the stratified layer. The effect of the unrealistically large vertical diffusivity will be taken into account when interpreting our results. The turbulent vertical diffusivity in the high salinity ocean is poorly constrained, as no energy is required to mix the unstratified ocean. The horizontal and vertical scale of the grid in our simulations are of similar order (10^3 m), so that an isotropic diffusion regime is plausible. However, due to the effect of gravity and rotation, highly anisotropic turbulent diffusion may also be justified. We have therefore performed simulations with both isotropic and anisotropic diffusion for the high salinity ocean. All viscosities are set by fixing $Pr = 10$.

We carry out 4 simulations to examine the influence of different factors on ocean circulation (Table 2). In order to examine the role of salinity, we carry out two simulations, *HSaniso* and *LSaniso*, with two different salinities: 8.5 g kg^{-1} for the low salinity case (Glein et al. (2018)) and 35 g kg^{-1} for

the high salinity case (similar to Earth's ocean). We perform simulations with both isotropic and anisotropic diffusion (*HSiso* versus *HSaniso*) in high salinity oceans to test the robustness of our results. The isotropic diffusion is consistent with Soderlund (2019), and the anisotropic diffusion is consistent with Kang et al. (2020), as well as with our low salinity simulation. In order to examine the influence of resolution, we set up a simulation with doubled horizontal resolution (*HSiso05* compared with *HSiso*). We only test the effect of resolution in the high salinity ocean because the low salinity ocean takes a much longer time to reach an equilibrium state, due to the diffusive adjustment of the stratified layer, which makes the simulation computationally very expensive. All simulations are integrated to a near equilibrium state in which the energy imbalance is less than 2%. The presented results are 10-year-averages for high salinity cases and 250-year-averages for the low salinity case after this equilibrium has been reached. The longer averaging time in the low salinity case was chosen to account for a much larger low-frequency variability in this simulation.

To study tracer mixing processes in the ocean, we carry out three tracer simulations initialized from the equilibrium states of *HSaniso*, *HSiso* and *LSaniso*. We initialize two passive tracers (i.e. with no effect on ocean density and thus dynamics) at the bottom of the ocean at 0° and 60°S to study the evolution of tracer concentration. The turbulent diffusivity for the tracers is set to be the same as the thermal turbulent diffusivity. Each tracer simulation is run for 1500 years, and 10-year-averages are used for analysis.

3.2. Simulation Results

3.2.1. Vertical Stratification and Circulation

In our high salinity simulations, the ocean is slightly negatively stratified at all depths, (Figure 5(a)-(c)), which indicates that convection can occur over the whole depth of the ocean. In *HSiso* and *HSiso05*, the resolved convection at mid- and high-latitudes is, however, weak (Figure 6(c), (f) & (i)). This result can be understood by noting that the large vertical diffusivity and viscosity in these two cases leads to a relatively low Rayleigh number ($Ra = \alpha g \delta T D^3 / \nu \kappa$ where δT is the temperature contrast between the bottom and surface of the ocean and ν is viscosity) of $Ra \approx 1 \times 10^6$ in *HSiso* and $Ra \approx 1.5 \times 10^7$ in *HSiso05*. Importantly, the Rayleigh number in these two cases is smaller than the critical value that has been suggested for rotating convection: $Ra_S = 8.7E^{-4/3}$ where $E = \nu / (2\Omega D^2)$ is the Ekman number (Cheng et al. (2018)). The critical Rayleigh number is $Ra_S \approx 2 \times 10^7$ in *HSiso* and $Ra_S \approx 8 \times 10^7$ in *HSiso05*. As a result, radial heat flux is dominated by the parameterized turbulent diffusion. Temperature gradients are very small in all high salinity simulations, with the whole ocean around the freezing point. The bottom to surface buoyancy contrast is $\alpha g \delta T \approx 10^{-7} \text{ m s}^{-2}$ in *HSaniso* and $\alpha g \delta T \approx 10^{-8} \text{ m s}^{-2}$ in *HSiso* and *HSiso05* (Figure 6(a), (d) & (g)). For comparison, the prescribed buoyancy contrast in Soderlund (2019) is around 10^{-5} m s^{-2} for Enceladus, which is at least two orders of magnitude larger than our result, consistent with a radial heat flux in the simulations of Soderlund (2019) that is many orders of magnitude larger than the observed surface heat loss.

The zonal flow at mid-latitudes is constrained by the temperature structure via the thermal wind relationship, in particular the equator-to-pole temperature gradient, with warmer temperatures at the poles and colder temperatures at low latitudes, which leads to a negative (westward) vertical current shear at mid-latitudes (second column in Figure 6). In *HSaniso*, there exists superrotation in the equatorial upper ocean (Figure 6(b)), while such superrotation does not exist in *HSiso* and

HSiso05 (Figure 6(e) & (h)), suggesting that the equatorial dynamics are sensitive to poorly constrained simulation parameters. The mechanism for the superrotation is associated with upward eddy momentum fluxes, consistent with previous studies (Aurnou & Olson (2001); Kaspi (2008); Ashkenazy & Tziperman (2020)) (see APPENDIX C for a more detailed discussion of the mechanism for superrotation). Note that the simulation results of *HSiso* and *HSiso05* with different resolutions are qualitatively similar but differ quantitatively (the 2nd and 3rd rows in Figure 6).

As predicted, there are two different vertical layers in the low salinity ocean (Figure 5(d)-(f)). The bottom layer is a convective layer, which is slightly negatively stratified with positive thermal expansivity and small temperature variation around the critical point T_c (Figure 5(e) & Figure 6(j)). In the time-averaged equilibrium state, convection in the convective layer in the low salinity ocean (Figure 6(l)) is weaker than in the high salinity ocean (Figure 6(c)), as expected due to the smaller thermal expansivity and thus smaller buoyancy input. The upper layer is the stratified layer with stable stratification and negative thermal expansivity, so that convection is blocked at the bottom of this layer (Figure 6(l)). The vertical temperature gradient is relatively large in this layer, with a profile that is linearly increasing from the freezing point T_f at the surface of the ocean to the critical temperature T_c at the interface between the two layers. We can apply Equation (1) to estimate the expected depth of the stratified layer. In our simulation, the temperature variation is $|\Delta T| \approx 2.0$ K, the vertical heat flux is $Q \approx 0.03$ W m², and the vertical thermal diffusivity is $\kappa_{z,heat} = 5 \times 10^{-5}$ m² s⁻¹, such that the predicted depth of the stratified layer is around 13 km. This estimated depth matches well with the simulation results (Figure 5(d)-(f)), although we note that the same estimate predicts a

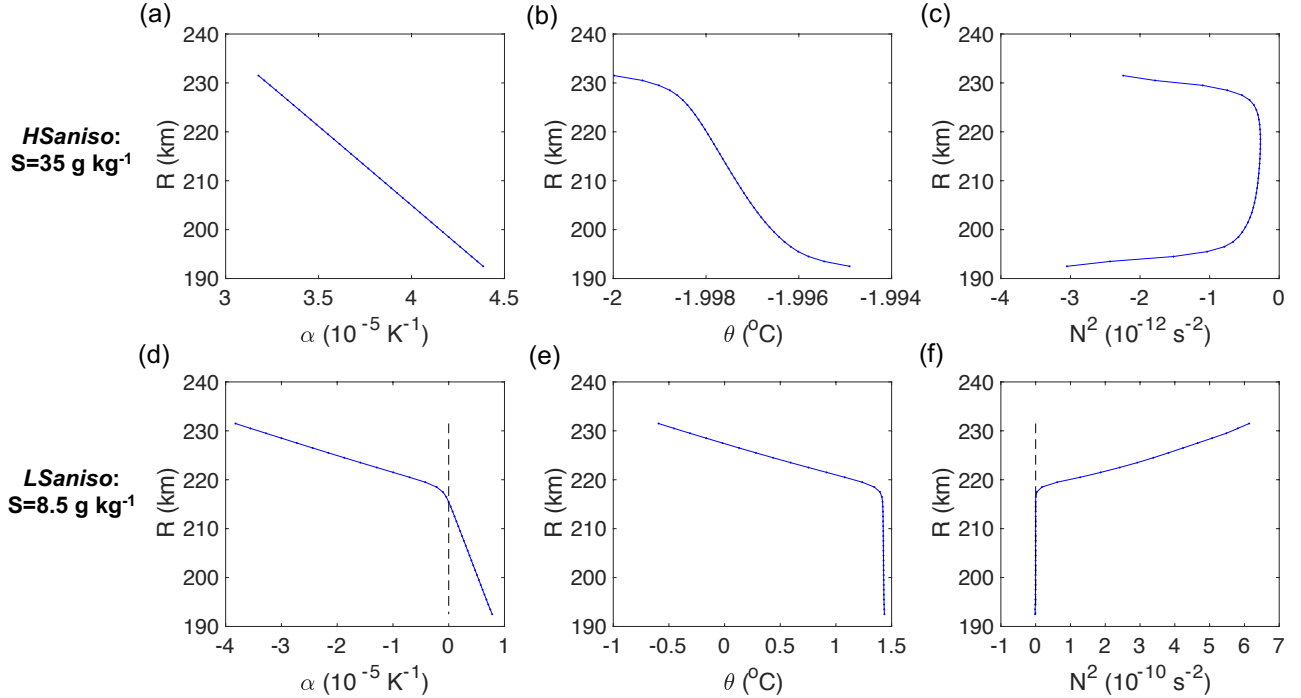


Figure 5. Vertical stratification of the high and low salinity ocean (top row and bottom row, respectively). From left to right are the horizontally averaged vertical profile of thermal expansivity α , potential temperature θ and stratification $N^2 \approx \alpha g \partial \theta / \partial z$. The black dashed line marks the zero-line.

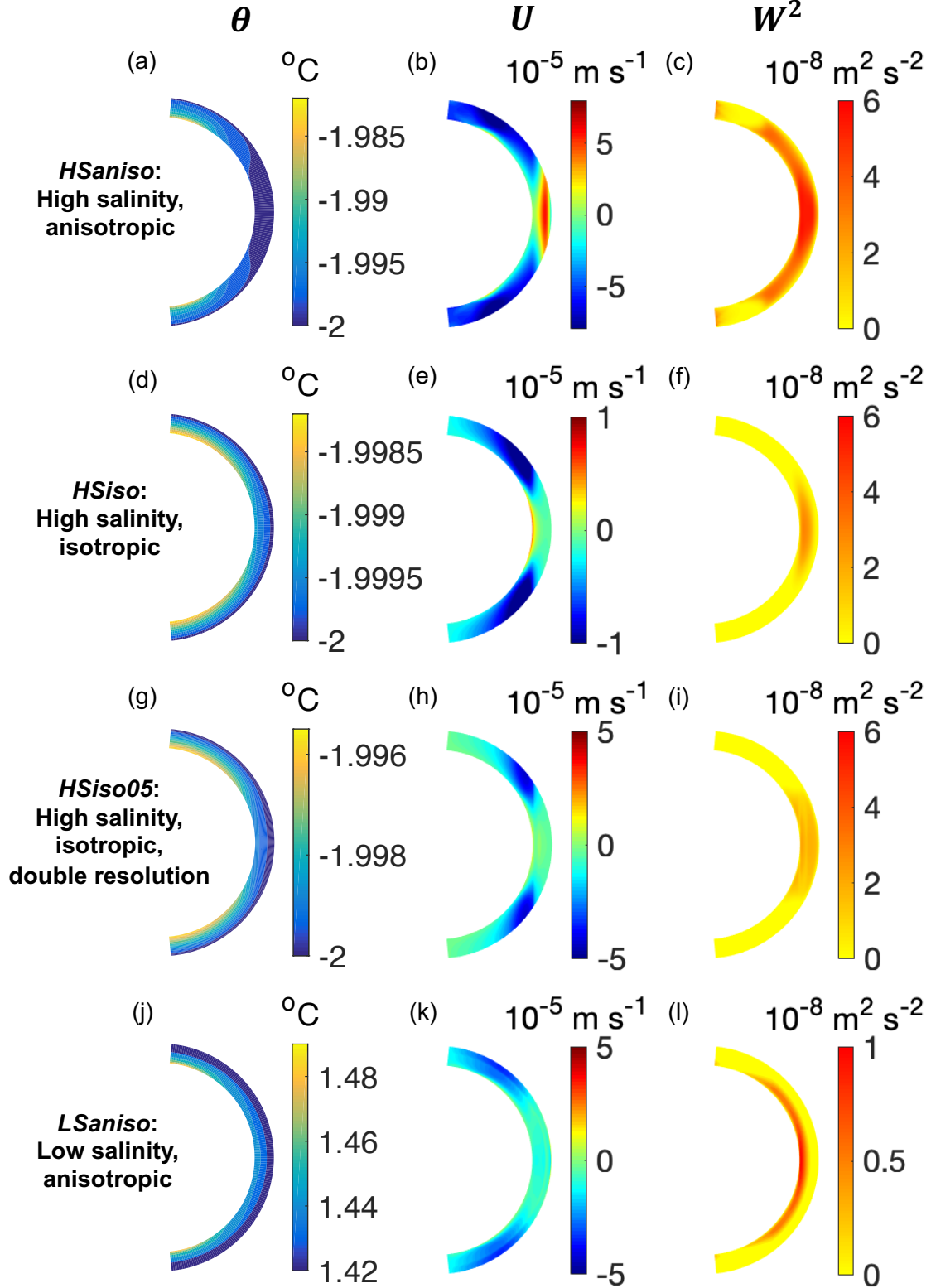


Figure 6. Ocean potential temperature and flow fields in the equilibrium state of different simulations. From left to right, the three columns show time-averaged zonal-mean fields of potential temperature θ , zonal velocity U and vertical kinetic energy W^2 , respectively. Note that the colorbar is saturated in panel (j). The surface temperature in *LSaniso* is very low (-0.6 °C) and increases with depth linearly in the stratified layer, as shown in Figure 5(e).

much shallower stratified layer for Enceladus, where the vertical diffusivity is expected to be weaker than in our simulations.

3.2.2. Ocean Heat Transport

The mechanisms governing ocean heat transport vary widely across our simulations. With anisotropic diffusivity and viscosity (*HSaniso*) the vertical heat flux in the high salinity simulation is dominated by explicitly resolved convection (Figure 7(a)). With isotropic diffusivity and viscosity (*HSiso* and *HSiso05*) instead, the vertical heat flux is dominated by parameterized turbulent diffusion (Figure 7(b) & (c)) due to the large vertical diffusivity.

The choice of anisotropic versus isotropic diffusivity and viscosity also affects the heat flux at the ice-ocean interface, and by comparing the ocean surface heat flux from simulation results with the idealized models in Section 2.3 we find that all three aspects—slantwise convection, radial diffusion and horizontal mixing—appear to play a role in different configurations. In *HSaniso*, there are peaks near the tangent cylinder, but the latitude of the peaks is located significantly further poleward than expected from the “slantwise convection” model, and the overall structure of the heat flux is significantly more complex, due to significant spatial variations in the magnitude and character of the convection (Figure 8(a)). Another difference from the idealized “slantwise convection” model is that heat flux outside the tangent cylinder (i.e. near the equator) is not small. This is due to vertical heat transport by “equatorial rolls”—convection cells at the equator, which have been discussed in Kang et al. (2020). Although the result that vertical heat transport is dominated by convection is

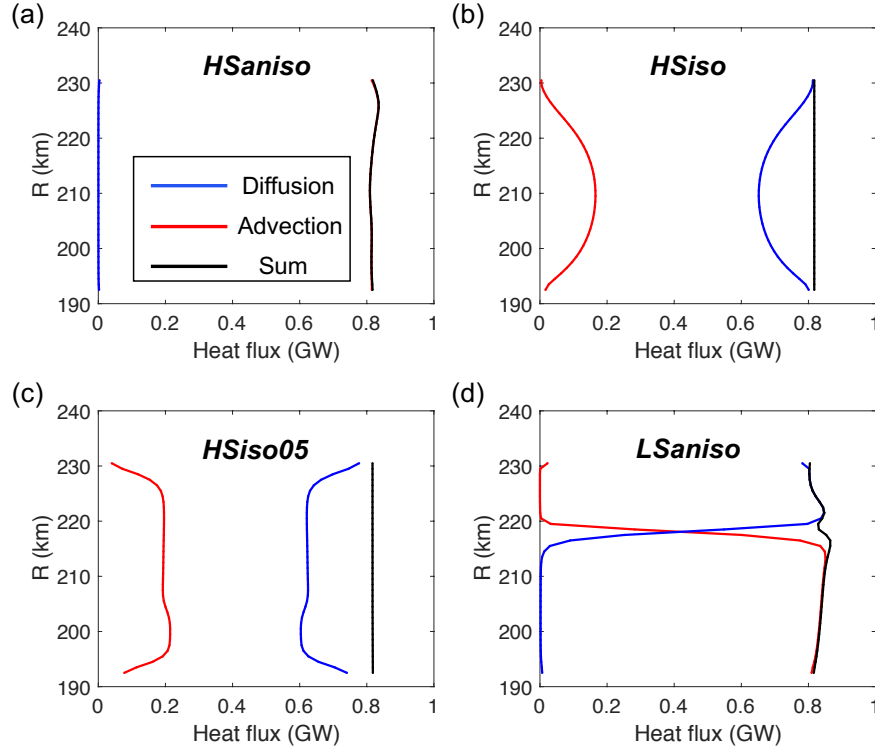


Figure 7. Vertical heat flux in the simulations. Panels show horizontally integrated vertical heat flux as a function of depth in *HSaniso* (a), *HSiso* (b), *HSiso05* (c), and *LSaniso* (d), respectively. Blue lines indicate the heat flux due to parameterized turbulent diffusion, red lines indicate the heat flux due to resolved advection, and black lines indicate the total heat flux.

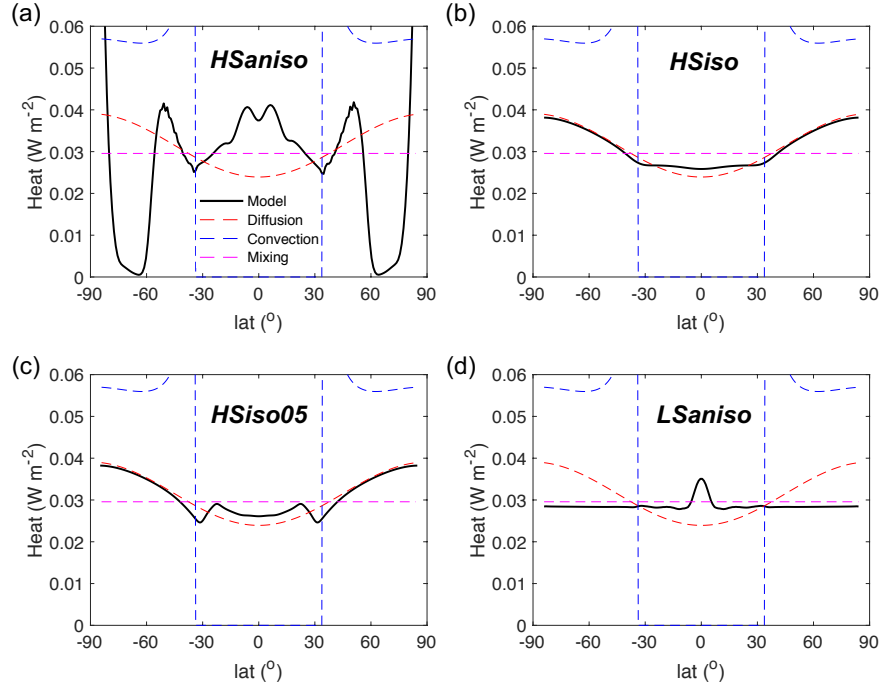


Figure 8. Ocean surface heat flux in simulations compared with three idealized models. Black lines indicate the surface heat flux in the simulations. Dashed lines indicate the surface heat flux in three idealized models, where red lines indicate the “radial diffusion” (Diffusion) model, blue lines indicate the “slantwise convection” (Convection) model and pink lines indicate the “strong horizontal mixing” (Mixing) model.

likely to be robust, the specific patterns of the convection are likely to depend on model resolution and poorly constrained parameters. In particular, the highly anisotropic viscosity and diffusion coefficients clearly affect the dynamics significantly. Although unresolved turbulence is likely to be anisotropic, even in a high salinity scenario, both the strength and alignment of the anisotropy remain unknown.³

In *HSiso* and *HSiso05*, the surface heat fluxes are very close to the “radial diffusion” model (Figure 8(b) & (c)), consistent with the result that vertical heat flux is dominated by parameterized isotropic turbulent diffusion. The heat flux at the equator is somewhat larger than predicted by the “radial diffusion” model because it is enhanced by heat transport through the “equatorial rolls”. In *HSiso05*, there are small peaks outside the tangent cylinder, which are caused by slantwise convection (c.f. Figure 6(i)). These peaks qualitatively resemble those predicted by the “slantwise convection” model, although their amplitude is very weak, due to the dominant role of diffusion.

In the low salinity case, *LSaniso*, the vertical heat transport is dominated by convection in the bottom convective layer, but is dominated by diffusion in the upper stratified layer (Figure 7(d)). The surface heat flux is almost uniform, and well approximated by the “strong horizontal mixing” model (Figure 8(d)). The approximately uniform surface heat flux is a result of the relatively strong horizontal mixing in the stably stratified layer where the horizontal diffusivity is much larger than the

³ Anisotropy can be imposed by gravity and/or rotation. Anisotropy brought about by gravity tends to align radially, while anisotropy due to rotation tends to align along the rotation axis (like Taylor columns). Our choice for the anisotropic viscosities, $\nu_r \gg \nu_h$, is only justified in the former regime.

vertical diffusivity. The peak at the equator is associated with grid-scale vertical advection, which is likely to be an artifact of numerical instability.

3.2.3. Ocean Tracer Mixing

The three tracer simulations illustrate the mixing processes in the ocean and the time scale it takes for any constituents to be mixed from the bottom to the surface of the ocean. In the high salinity ocean, tracers can reach the surface of the ocean within tens of years. The convective mixing time scale is within an order of magnitude but somewhat shorter than the estimate according to

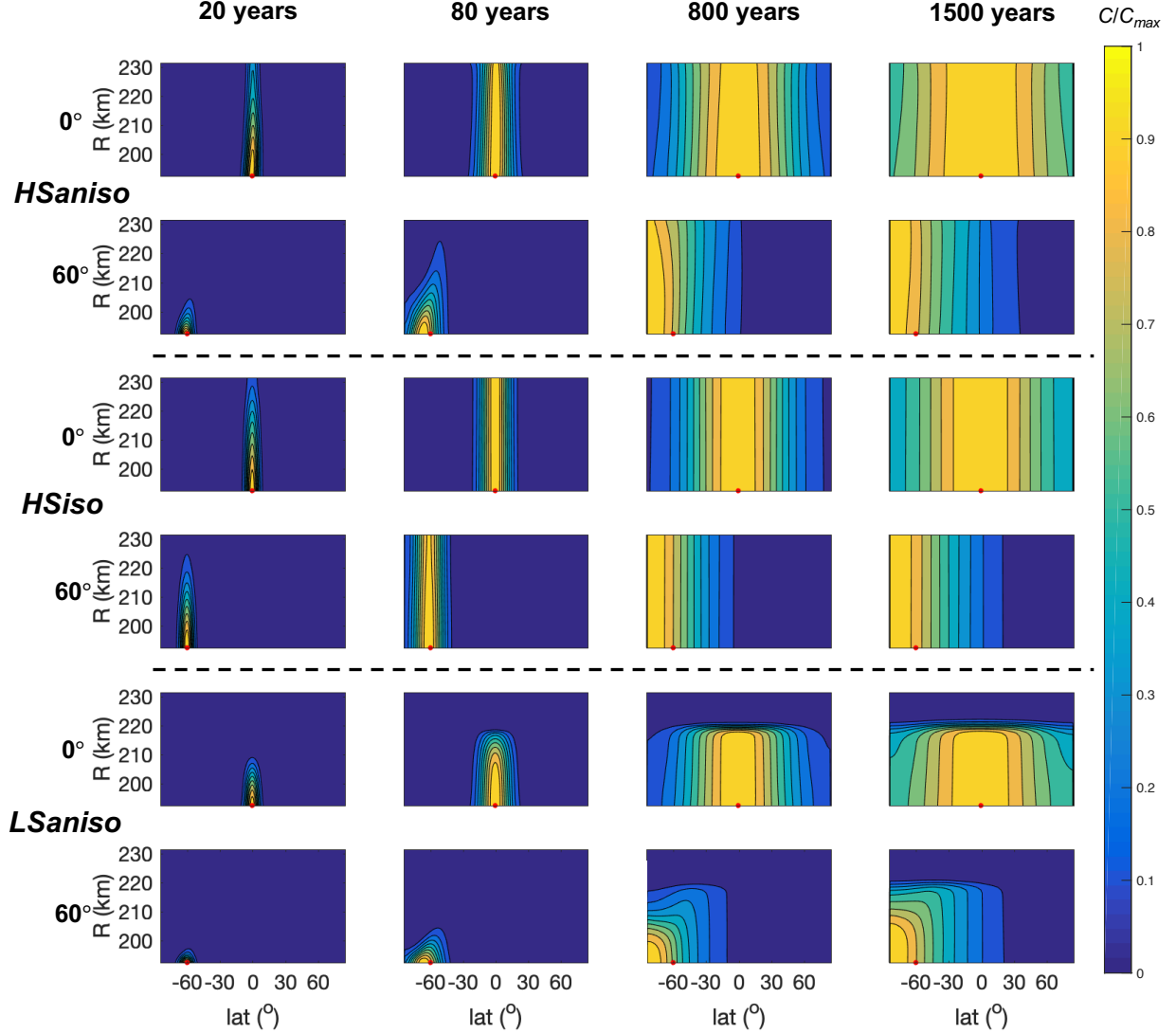


Figure 9. Zonally-integrated tracer concentration as a function of latitude and depth. The concentration is normalized by the maximum value in each plot. From top to bottom, rows show simulation results in which the tracer is initialized at the ocean floor at 0° and 60°S (the red dots in each panel) in *HSaniso*, *HSiso*, and *LSaniso*, respectively. From left to right, columns show 10-year-averages after 20, 80, 800 and 1500 years, respectively.

Equation (4) because our model cannot adequately resolve the convective plumes and the scaling underestimates the vertical velocities in the simulations. Horizontal mixing across the hemisphere takes around 1000 years, while global mixing across the equator remains incomplete by the end of our 1500-year simulation (Figure 9). The mixing time scales are only moderately dependent on the choice of isotropic versus anisotropic diffusion. Note that the poleward drift of the highest concentration center and the tilting pattern arise due to spherical geometry effects on the diffusive transport as well as advection by meridional currents.

In the low salinity simulation, *LSaniso*, the mixing time scale in the bottom convective layer is similar to that in the high salinity simulations. However, the tracers do not penetrate significantly into the stratified layer, even after 1500 years (Figure 9). The vertical mixing time scale in the stratified layer can be estimated using Equation (6). In our simulation, $\kappa_{z,heat} = \kappa_{z,tracer} = 5 \times 10^{-5} \text{ m}^2 \text{ s}^{-1}$, so that $\tau_{diff} \approx 4 \times 10^{12} \text{ s} \approx 1 \times 10^5 \text{ years}$. This is consistent with the simulation results showing little tracer penetration into the stratified layer after 1500 years, although we note that this time scale is likely to be too large in our simulations due to the unrealistically large vertical diffusivity (c.f. Equation (6)). As we discussed in Section 2.4, we estimate that the vertical mixing time scale in the stratified layer for parameters representative of Enceladus' ocean should be between several hundreds to several tens of thousands of years.

4. CONCLUSION

We find that the salinity of Enceladus' ocean fundamentally determines the vertical stratification and circulation of the ocean, thereby affecting the heat and tracer transport from the rocky core to the surface ice shell. If salinity is high, the ocean is unstratified and is dominated by convection over the whole depth. Tracers can be transported from the bottom to the surface within tens of years. In a low salinity ocean (below a critical point of about 20 g kg^{-1}), a stably stratified layer exists in the upper ocean, which strongly suppresses vertical mixing, leading to a vertical mixing time scale between hundreds and tens of thousands of years. In the presence of significant horizontal mixing, the stratified layer further leads to horizontally homogeneous heat transport to the ice shell, independent of any spatial structure in the heat flux underneath. More detailed simulation results are sensitive to model resolution, as well as the magnitudes of the assumed turbulent viscosities and diffusivities, which remain poorly constrained.

Our simulations are based on an ocean-only model, hence the effect of freezing and melting on salinity as well as variations in the ice thickness are not included. Future work is required to investigate dynamics of the ocean on Enceladus when the ocean is coupled with an ice shell of spatially varying thickness. However, care must be taken in any such study to investigate the sensitivity of the results to model parameters and resolution, which are always based on compromises enforced by limited computational resources.

Our results indicate a contradiction in estimates of salinity and vertical mixing time scale of Enceladus' ocean in previous studies. Studies on the geochemistry of Enceladus' ocean have generally indicated a relatively low salinity, likely less than 20 g kg^{-1} (Glein et al. (2018)). In this case we expect a stably stratified layer to form and result in a vertical mixing time scale between the rocky sea floor and the ice shell of at least hundreds of years. However, the detection of silica nanoparticles in plumes has been argued to set an upper limit of several years on the mixing time scale, based on the size and growth rate of the particles (Hsu et al. (2015)). Our results suggest that these inferences

are not compatible with each other, indicating that Enceladus' ocean is either saltier than previously suggested or the interpretation of silica nanoparticles needs to be reconsidered.

ACKNOWLEDGMENTS

We are grateful to Jun Yang, Edwin S. Kite, Wanying Kang and Dorian S. Abbot for helpful discussions and comments. Y.Z. thanks the Department of Atmospheric and Oceanic Sciences and School of Physics in Peking University for the financial support during the summer exchanging program in University of Chicago. This work was completed with resources provided by the University of Chicago Research Computing Center.

APPENDIX

A. CALCULATION OF SURFACE HEAT FLUXES IN THREE CONCEPTUAL MODELS

In this part, we will explain the calculation of surface heat fluxes in the three conceptual models shown in Figure 3.

In the “slantwise convection” model, we relate points at the ocean-ice interface to those on the sea floor that lie on the same line parallel to the axis of rotation (Figure 10):

$$r_t \cos \theta_t = r_b \cos \theta_b, \quad (\text{A1})$$

where the subscript t indicates the top of the ocean and the subscript b indicates the bottom of the ocean, r is radius and θ is latitude. Setting $\theta_b = 0$ we can solve for the latitude of the tangent cylinder at the top of the ocean:

$$|\theta_t^c| = \cos^{-1}(r_b/r_t). \quad (\text{A2})$$

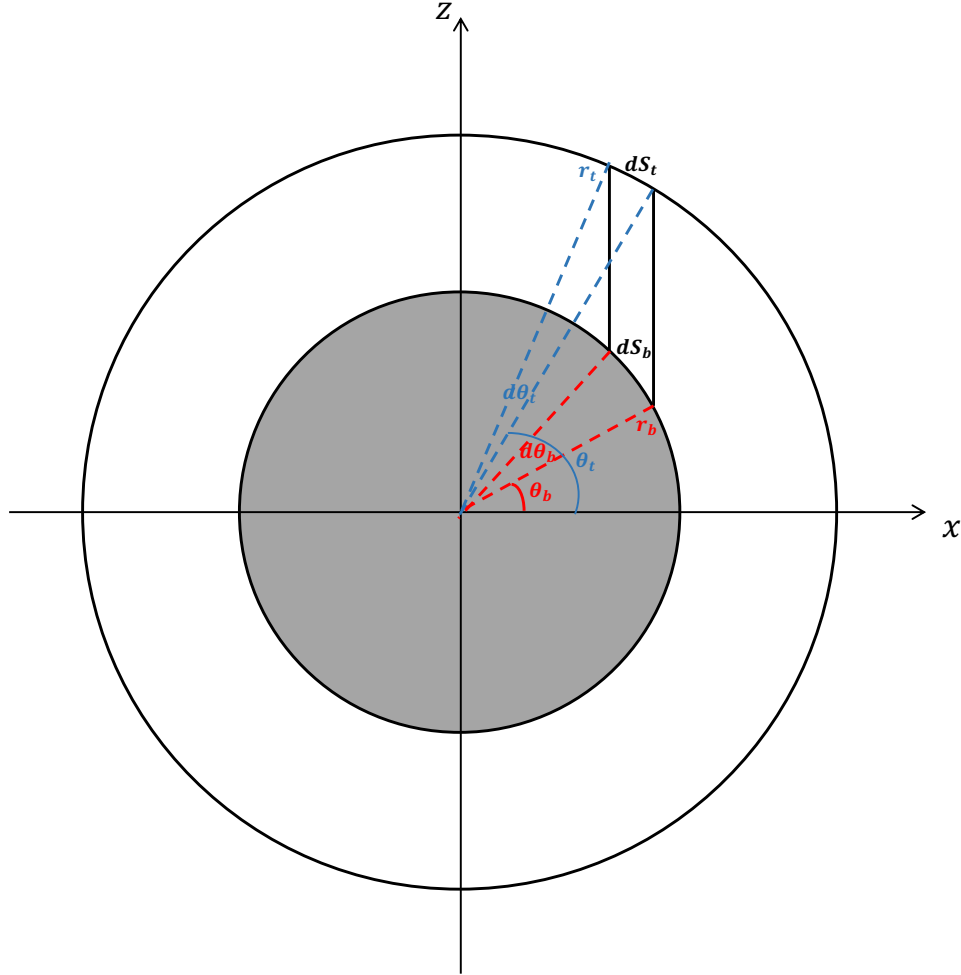


Figure 10. Schematic for the “slantwise convection” model. The rotation axis is the z -axis, and other symbols are explained in the text.

If the bottom heating is entirely transported to the surface by the columnized convection, we moreover find

$$Q_b(\theta_b)r_b^2 \cos \theta_b d\theta_b d\lambda = Q_t(\theta_t)r_t^2 \cos \theta_t d\theta_t d\lambda \quad (\text{A3})$$

where Q is the heat flux. From Equation (A1) we get $d\theta_b/d\theta_t = (r_t \sin \theta_t)/(r_b \sin \theta_b)$, so that Equation (A3) can be solved for the heat flux at the ocean surface, $Q_t(\theta_t)$, inside the tangent cylinder. The surface heat flux is zero outside the tangent cylinder, so that it can generally be written as

$$Q_t(\theta_t) = \begin{cases} 0, & \text{if } |\theta_t| < |\theta_t^c|, \\ Q_b(\theta_b) \frac{\sin \theta_t}{\sin \theta_b}, & \text{if } |\theta_t| > |\theta_t^c|, \end{cases} \quad (\text{A4})$$

where θ_b is determined by Equation (A1) and θ_t^c is given by Equation (A2). Notice that Equation (A4) has a singularity at the latitude where the surface intersects with the tangent cylinder.

In the “radial diffusion” model, heat fluxes at the sea floor can be matched directly to surface fluxes at the same latitude, reduced only by a factor that accounts for the radial increase in surface area:

$$Q_t(\theta) = Q_b(\theta) \frac{r_b^2}{r_t^2}. \quad (\text{A5})$$

In the “strong horizontal mixing” model, the surface heat flux is independent of latitude and simply given by the total heat flux divided by the surface area:

$$Q_t(\theta) = \frac{2\pi \int_{-\pi/2}^{\pi/2} Q_b(\theta') r_b^2 \cos \theta' d\theta'}{4\pi r_t^2}. \quad (\text{A6})$$

B. ADDITIONAL SIMULATION DETAILS

Due to the deep ocean (40 km) compared to the planetary radius (252 km), our GCM simulations do not use the thin-shell approximation typically applied in Earth-like simulations (MITgcm Manual, Adcroft et al. (2018)). As a result, the variation of grid cell area with depths at the same latitude and longitude is taken into consideration, which allows vertical fluxes to be calculated more precisely. The vertical variation of gravity is also taken into account. We calculate the gravity as a function of depth as

$$g(r) = g_c \frac{r_c^2}{r^2} + \frac{4\pi G \rho_w}{r^2} \int_{r_c}^r r'^2 dr', \quad (\text{B1})$$

where G is the gravitational constant, r_c is the radius at the surface of the solid core, i.e. the bottom of the ocean, $\rho_w = 1000 \text{ kg m}^{-3}$ is the density of water (and also ice, for simplicity) and $g_c = 0.127 \text{ m s}^{-2}$ is the gravity at the bottom of the ocean, chosen such as to keep the gravity at the surface of the ice shell $g(r_s)$ to be the observed value of 0.113 m s^{-2} . The vertical profile of the gravity is shown in Figure 4(a).

The bottom tidal heating pattern is expected to reflect the tidal disturbing potential. By further assuming that the global total energy input is 20 GW, and the maximum heat flux is twice of the minimum (Choblet et al. (2017)), the heating pattern is suggested to be:

$$Q_{core}(\Theta, \lambda) = \frac{F_{total}[1/2 Y_{20}(\Theta) - 1/4 Y_{22}(\Theta, \lambda) + C_0]}{4\pi C_0 r_c^2}, \quad (\text{B2})$$

where $F_{total} = 20$ GW is the total tidal heating, $C_0 = (0.5 + \sqrt{3}/8) \sqrt{5/\pi} \approx 0.904$ is a constant, Θ is co-latitude, λ is longitude, and Y_{20} and Y_{22} are degree-2 spherical harmonic functions. Since we are only simulating part of the zonal range of the global ocean (15° in longitude), we cannot adequately simulate zonal variations. We therefore apply a zonally symmetric heating profile given by the zonal mean of Equation (B2), which is (Figure 4(b)):

$$Q_{core}(\Theta) = \frac{F_{total}[1/2 Y_{20}(\Theta) + C_0]}{4\pi C_0 r_c^2}. \quad (\text{B3})$$

In simulations with varying horizontal resolution, the viscosity coefficient is modified such that the Kolmogorov scale is proportional to the grid scale (Vallis (2017)). The Kolmogorov scale L_ν is the length scale at which the viscosity becomes important, and scales as:

$$L_\nu \sim \varepsilon^{-1/4} \nu^{3/4}, \quad (\text{B4})$$

where ε is the turbulent energy cascade rate, which should be independent of resolution, and ν is the turbulent viscosity. Setting $L_\nu \sim L_{grid}$, we can get the relationship:

$$\nu \propto L_{grid}^{4/3}. \quad (\text{B5})$$

We here choose L_{grid} as the horizontal grid scale, which in our model is generally larger than the vertical grid scale. The horizontal grid length in case *HSiso05* is half of that in case *HSiso*, so that the viscosity is correspondingly changed from $2.5 \text{ m}^2 \text{ s}^{-1}$ to $2.5 \times 0.5^{4/3} \approx 1.0 \text{ m}^2 \text{ s}^{-1}$. We set other parameters in case *HSiso05* by keeping the diffusivity and viscosity isotropic and $Pr=10$ (Table 2).

C. MECHANISMS FOR SUPERROTATION

There exists superrotation in the upper ocean in *HSaniso* but not in *HSiso* and *HSiso05*. Here we compare *HSaniso* and *HSiso* to analyze the mechanism for equatorial superrotation. The two isotropic simulations, *HSiso* and *HSiso05*, are similar (not shown).

The zonal-mean zonal momentum budget is (Vallis (2017)):

$$\begin{aligned} \frac{\partial \bar{u}}{\partial t} = & 2\Omega(\bar{v} \sin \theta - \bar{w} \cos \theta) \\ & + \overline{F_x} \\ & - \frac{v}{a \cos \theta} \frac{\partial}{\partial \theta} (\bar{u} \cos \theta) - \bar{w} \frac{\partial \bar{u}}{\partial r} - \frac{\overline{uw}}{r} + \frac{\overline{uv \tan \theta}}{r}, \end{aligned} \quad (\text{C1})$$

where the overbar indicates the zonal and temporal average; u , v , w are zonal, meridional and vertical velocity, respectively; θ is latitude, and F_x is dissipation. On the right-hand-side, the terms in the first line are the Coriolis force, the term in the second line is the dissipation, and the terms in the third line are the advection terms (including metric terms). In an equilibrium state, the left-hand-side should be zero.

Superrotation in *HSaniso*, which is largest around $r = 219$ km (around 13 km in depth), is driven by momentum flux convergence (Figure 11(c)) and counteracted by Coriolis terms and frictional dissipation (Figure 11(a) & (b)). In *HSiso*, however, such a momentum flux convergence is absent. A cross section of vertical velocity along the equator (Figure 11(d)) shows that the upward momentum

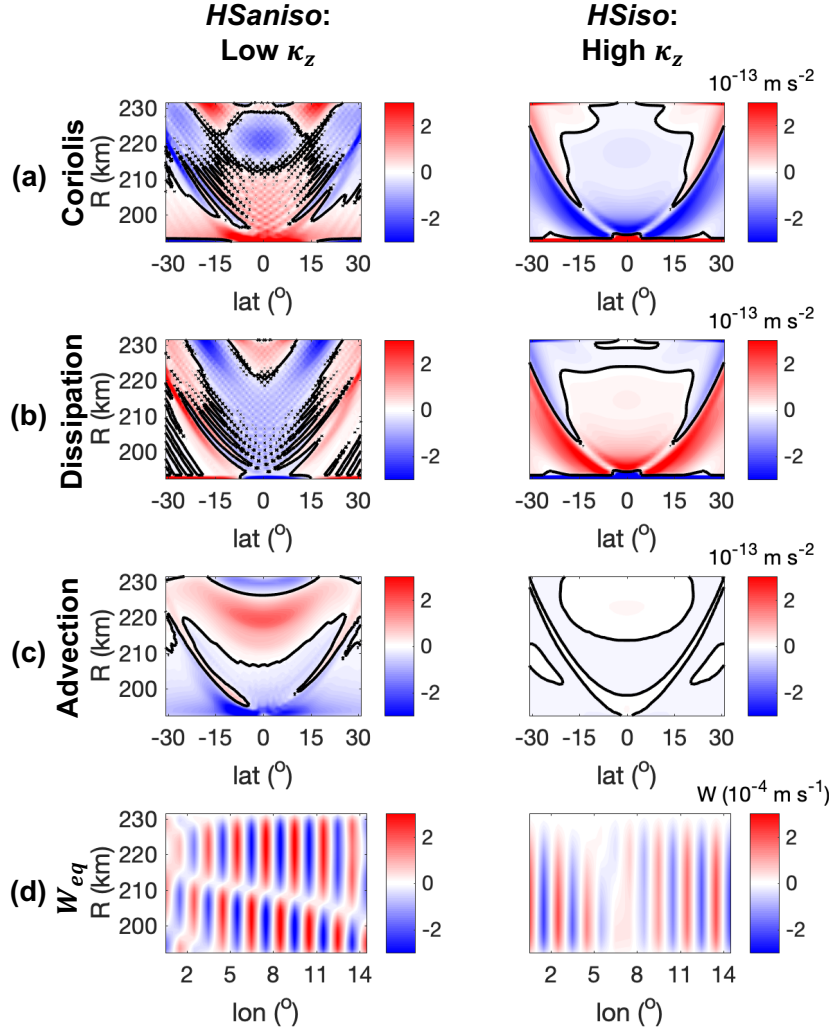


Figure 11. Momentum budget and equatorial eddies in *HSaniso* (left) and *HSiso* (right). Panels (a)-(c) show ten-year-averaged zonal-mean zonal acceleration due to Coriolis force, dissipation, and advection terms, respectively. Black lines in (a)-(c) are zero contour lines. Panel (d) shows snapshots of vertical velocity in the equatorial plane. Note that the equatorial convective patterns are grid-scale because the horizontal resolution is not able to resolve the intrinsic scale of the convective plumes, but within the constraint imposed by this limitation, the equatorial velocity structure in *HSaniso* shows a vertical tilt, which is associated with upward momentum transport.

flux in *HSaniso* is driven by vertically tilted eddies (Aurnou & Olson (2001); Kaspi (2008)). Although similar eddies appear to exist in *HSiso*, they are weaker and not tilted, and hence do not carry momentum upwards.

REFERENCES

- Adcroft, A., Jean-Michel, C., Stephanie, D., et al. 2018, MITgcm User Manual, Tech. rep., online documentation: <https://mitgcm.readthedocs.io/en/latest/>
- Amit, H., Choblet, G., Tobie, G., et al. 2020, Icarus, 338, 113509
- Ashkenazy, Y., Sayag, R., & Tziperman, E. 2018, Nature Astronomy, 2, 43

- Ashkenazy, Y., & Tziperman, E. 2020, arXiv preprint arXiv:2006.02242
- Aurnou, J. M., & Olson, P. L. 2001, *Geophysical research letters*, 28, 2557
- Beuthe, M. 2016, *Icarus*, 280, 278
- . 2019, *Icarus*, 332, 66
- Čadek, O., Souček, O., Běhouňková, M., et al. 2019, *Icarus*, 319, 476
- Cardin, P., & Olson, P. 1994, *Physics of the earth and planetary interiors*, 82, 235
- Chen, E., & Nimmo, F. 2011, *Icarus*, 214, 779
- Chen, E., Nimmo, F., & Glatzmaier, G. 2014, *Icarus*, 229, 11
- Cheng, J. S., Aurnou, J. M., Julien, K., & Kunnen, R. P. 2018, *Geophysical & Astrophysical Fluid Dynamics*, 112, 277
- Choblet, G., Tobie, G., Sotin, C., et al. 2017, *Nature Astronomy*, 1, 841
- Christensen, U. R. 2002, *Journal of Fluid Mechanics*, 470, 115
- Fofonoff, N. P., & Millard Jr, R. 1983, *UNESCO Technical Papers in Marine Science*, 44, 53
- Glein, C., Postberg, F., & Vance, S. 2018, *Enceladus and the icy moons of Saturn*, 39
- Goodman, J. C., Collins, G. C., Marshall, J., & Pierrehumbert, R. T. 2004, *Journal of Geophysical Research: Planets*, 109
- Goodman, J. C., & Lenferink, E. 2012, *Icarus*, 221, 970
- Hay, H. C., & Matsuyama, I. 2017, *Icarus*, 281, 342
- . 2019, *Icarus*, 319, 28
- Hemingway, D. J., & Mittal, T. 2019, *Icarus*, 332, 111
- Howett, C., Spencer, J., Pearl, J., & Segura, M. 2011, *Journal of Geophysical Research: Planets*, 116
- Hsu, H.-W., Postberg, F., Sekine, Y., et al. 2015, *Nature*, 519, 207
- Ingersoll, A. P., & Nakajima, M. 2016, *Icarus*, 272, 319
- Jackett, D. R., & McDougall, T. J. 1995, *Journal of Atmospheric and Oceanic Technology*, 12, 381
- Jansen, M. F. 2016, *Journal of Physical Oceanography*, 46, 1917
- Jones, H., & Marshall, J. 1993, *Journal of Physical Oceanography*, 23, 1009
- Kang, W., Bire, S., Campin, J.-M., et al. 2020, arXiv preprint arXiv:2008.03764
- Kang, W., & Flierl, G. 2020, *Proceedings of the National Academy of Sciences*, 117, 14764
- Kaspi, Y. 2008, PhD
- Kite, E. S., & Rubin, A. M. 2016, *Proceedings of the National Academy of Sciences*, 113, 3972
- Lobo, A. H., Thompson, A. F., Vance, S. D., & Tharimena, S. 2020, arXiv preprint arXiv:2007.06173
- Matsuyama, I., Beuthe, M., Hay, H. C., Nimmo, F., & Kamata, S. 2018, *Icarus*, 312, 208
- Melosh, H., Ekholm, A., Showman, A., & Lorenz, R. 2004, *Icarus*, 168, 498
- Munk, W., & Wunsch, C. 1998, *Deep-sea research. Part I, Oceanographic research papers*, 45, 1977
- Patthoff, D. A., & Kattenhorn, S. A. 2011, *Geophysical Research Letters*, 38
- Soderlund, K., Schmidt, B., Wicht, J., & Blankenship, D. 2014, *Nature Geoscience*, 7, 16
- Soderlund, K. M. 2019, *Geophysical Research Letters*, 46, 8700
- Souček, O., Běhouňková, M., Čadek, O., et al. 2019, *Icarus*, 328, 218
- Spencer, J., Howett, C., Verbiscer, A., et al. 2013, *EPSC Abstracts*, 8, 840
- Spencer, J., Pearl, J., Segura, M., et al. 2006, *science*, 311, 1401
- Thomas, P., Tajeddine, R., Tiscareno, M., et al. 2016, *Icarus*, 264, 37
- Tyler, R. 2011, *Icarus*, 211, 770
- Vallis, G. K. 2017, *Atmospheric and oceanic fluid dynamics* (Cambridge University Press), 413–441
- Wunsch, C., & Ferrari, R. 2004, *Annu. Rev. Fluid Mech.*, 36, 281
- Yang, J., Jansen, M. F., Macdonald, F. A., & Abbot, D. S. 2017, *Geology*, 45, 615